applied optics

Extended focused imaging and depth map reconstruction in optical scanning holography

ZHENBO REN, NI CHEN, AND EDMUND Y. LAM*

Department of Electrical and Electronic Engineering, The University of Hong Kong, Pokfulam, Hong Kong
**Corresponding author: elam@eee.hku.hk*

Received 10 December 2015; revised 6 January 2016; accepted 7 January 2016; posted 7 January 2016 (Doc. ID 255353); published 8 February 2016

In conventional microscopy, specimens lying within the depth of field are clearly recorded whereas other parts are blurry. Although digital holographic microscopy allows post-processing on holograms to reconstruct multifocus images, it suffers from defocus noise as a traditional microscope in numerical reconstruction. In this paper, we demonstrate a method that can achieve extended focused imaging (EFI) and reconstruct a depth map (DM) of three-dimensional (3D) objects. We first use a depth-from-focus algorithm to create a DM for each pixel based on entropy minimization. Then we show how to achieve EFI of the whole 3D scene computationally. Simulation and experimental results involving objects with multiple axial sections are presented to validate the proposed approach.

OCIS codes: (090.1995) Digital holography; (100.2000) Digital image processing; (100.3010) Image reconstruction techniques; (180.6900) Three-dimensional microscopy.

http://dx.doi.org/10.1364/AO.55.001040

1. INTRODUCTION

Optical microscope has been considered one of the most useful tools in biology and medicine for a long time. Among the different types of microscopy techniques, digital holographic microscopy (DHM) is unique in recording the light wavefront information originating from a three-dimensional (3D) object, instead of its projected image. Numerical reconstruction makes DHM more flexible in acquiring different kinds of images with proper algorithms. In the present work, we are concerned with a specific form of DHM called optical scanning holography (OSH), which is capable of imaging fluorescent specimens, making it particularly suitable for biological microscopy applications [1].

In OSH, the volume information of a 3D object, which contains multiple sections, is digitally recorded with an active 2D lateral scanning procedure on a photodetector. With the 2D digital hologram, the reconstruction is realized numerically to obtain the object's sectional information. However, similar to a traditional optical microscope, OSH suffers from the same problem of a limited depth of field (DOF). In conventional reconstruction, the recorded multiple sections cannot be sharp at the same time. In numerical reconstruction, when one particular section is focused, the other sections will manifest as defocus noise contaminating the reconstruction result. One solution to handle this problem is to suppress the defocus noise so that the slice we want to observe is clear and sharp. Wiener filter [2], Wigner distribution function [3], and inverse imaging approach [4,5] have been proposed to recover sectional information within the DOF. These methods are termed sectioning because they try to recover one specific sectional information while rejecting other sections. However, for applications such as microscopy and biology, we may not necessarily want to discard the information of other sections, but the whole scene should be clear enough for visualization and further analysis. Besides, knowing the depth information of each section of the 3D object is particularly useful to reconstruct a 3D model to understand the mechanism and surface morphology of microscopic specimens. Consequently, creating one single image where all sections along the longitudinal axis are brought to focus and reconstructing a depth map (DM) that gives the specific depth information of each section are very challenging but important tasks.

To achieve such extended focused imaging (EFI), exhibiting all sectional information of the object without corruption by out-of-focus noise that degrades the contrast and resolution, two major approaches have been proposed. The first is based on a specially designed phase plate, which is termed wavefront coding. In the optical path of a microscope, such a phase plate will facilitate an extension of the DOF of the images observed and magnified by the microscope [6]. Two-pupil synthesis in [7] can also be regarded as a specific kind of wavefront coding approach. The alternative solution constructs a single EFI image from a series of images obtained by mechanically scanning the 3D object on different sections, which is called focus

stacking. However, both approaches have drawbacks. For the former, the custom phase plate has to be fabricated and put along the optical path of the imaging system. Apart from the expected phase alterations, undesired aberration in optics and calibration for optical path increase the experimental complexity. The second method synthesizes an EFI image using photomontage. However, to acquire a stack of images in which each section is focused one by one for montage, multiple scanning steps, and precise movements and calibrations for each single-image acquisition pose severe limitations, consequently confining the application of this method [8].

As for the DM, the depth information plays an important role in object recognition and scene interpretation for the reconstruction of a 3D scene. Typically, the DM image is reconstructed by either stereoscopic matching [9] or depth-sensing devices such as a laser scanner and a time-of-flight sensor with direct scanning [10]. However, stereoscopic matching needs multiple-view images that record the same scene from different viewpoints with a slight stereo disparity. It fails when the objects in the region of interest are occluded, as well as for dynamic scenes. The direct laser scanning method requires additional device to scan the static scene with a laser beam or infrared light. These laser scanning devices are typically not applicable for microscopic specimens in biology.

In this paper, we present an algorithm to construct the EFI and DM images from a collection of digital holographic reconstructions in OSH. First, we create a DM by using a depth-from-focus algorithm, which recovers depth information by measuring focus based on entropy minimization, for each pixel. With this DM image, we can reconstruct the 3D scene of the recorded object. We then combine the DM and the collection of reconstructions together to create the EFI by selecting the in-focus values for every pixel.

2. PRINCIPLE OF FOCUS DETECTION IN OSH

A. OSH Imaging System

The schematic diagram of the OSH imaging system is shown in Fig. 1(a). A 2D scanner actively scans the 3D specimen along a predesigned trajectory. The transmitted light is collected and demodulated with heterodyne detection, as the real and imaginary parts of a complex hologram. Thus, a 2D digital hologram containing the entire 3D information of the object is obtained [4].

For the sake of mathematical simplicity, we model a 3D object as a stack of slices discretely distributed in space. In our simulation, all the sections are modeled as opaque planes with transparent areas, as shown in Figs. 1(b) and 1(c). We assume that the 3D object is expressed as $\sum_{i=1}^{\mathcal{K}} \mathcal{O}(x, y; z_i)$, where $\mathcal{K}$ is the total number of sections, (x, y) are spatial coordinates, and z_i is the distance of each section. Since OSH can be considered a linear space-invariant imaging system, with the help of the point-spread function (PSF), the hologram $g(x, y)$ can be computed as $g(x, y) = \sum_{i=1}^{\mathcal{K}} |\mathcal{O}(x, y; z_i)|^2 * h(x, y; z_i)$, where $*$ denotes 2D convolution and $h(x, y; z_i)$ is the PSF at z_i. Note that the 3D intensity transmittance of the object is encoded into the hologram, referred to as the incoherent-mode OSH, which enables the recording of a fluorescent specimen.

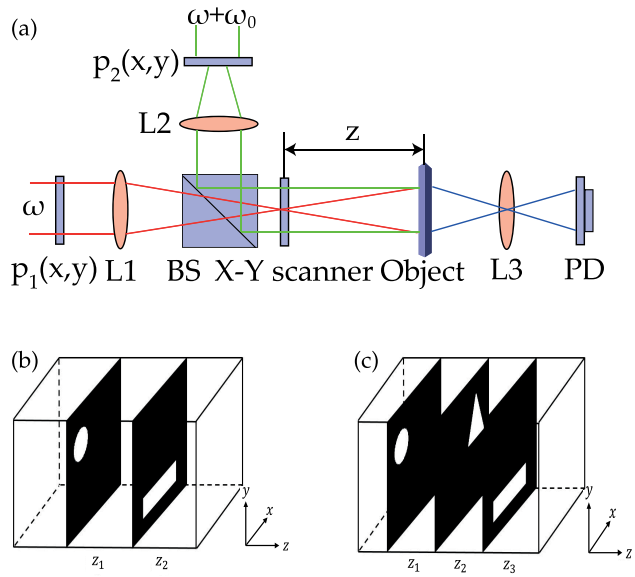

Fig. 1. (a) Schematic diagram of OSH imaging system. ω and ω_0 are the initial carrier frequency of the laser source and the shifted frequency, respectively; $p_1(x, y)$ and $p_2(x, y)$ are pupils; L1, L2, and L3 are lenses; BS is the beam splitter; X–Y scanner is a 2D scanning mirror; Object is the recorded specimen; PD is a photodetector; and z is the distance between the object and the scanner. (b) An object with two sections of a "circle" and a "rectangle" at z_1 and z_2, respectively. (c) An object with three sections of a "circle," a "triangle," and a "rectangle" at z_1, z_2, and z_3, respectively.

Conventional reconstruction deconvolves the hologram $g(x, y)$ with the conjugate PSF $h^*(x, y; z)$ to reconstruct individual sections. Mathematically, the reconstructed sectional image $r(x, y; z_1)$ at z_1 can be represented as [4]

$$\begin{aligned} r(x, y; z_1) &= g(x, y) * h^*(x, y; z_1) \\ &= |\mathcal{O}(x, y; z_1)|^2 + |\mathcal{O}(x, y; z_2)|^2 * h(x, y; z_2 - z_1), \end{aligned} \tag{1}$$

where $h(x, y; z_2 - z_1) = h(x, y; z_2) * h^*(x, y; z_1)$. Typically we discard the imaginary part of the reconstruction $r(x, y; z)$ as there is no signal content. The real part of the second term in Eq. (1) is regarded as defocus noise.

B. Focus Detection

For an imaging system, the DOF is usually limited. Within the DOF, the captured images are in focus and sharp. On the contrary, outside the DOF, image quality decreases gradually with distance from the focal plane of the lens. The DOF is not merely subject to the objective of the imaging system. It is affected by several factors, such as the focal length and the size of the lens, the distance between the lens and the object, the image sensor format, etc. Since an EFI image is a gathering of all in-focus parts, at the same time discarding the out-of-focus parts, it is essential to detect the focal distance from the reconstructed images [11].

In recent years, many methods have been proposed to find the focal distance within a scene. In image processing, focus metrics such as variance [12], correlation [13], gradient [14],

and contrast [15] are used to measure the sharpness of an image for assessing standard microscopy images. Fresnelet bases [16], spectral ℓ_1 norms [17], and Wigner distribution [18] are also used to extract the distance parameter by either expressing the optical signal as a sum of basis functions, or calculating the spectral content and filtering of the hologram. Computational imaging techniques such as changing the camera aperture [19] and estimating depth from the image structure [20] have also been proposed. In our approach, focus detection is efficiently computed based on entropy minimization. Although Chen *et al.* [21] already reported its use in digital holography, they worked on particle field in conventional coherent holography, and so incoherent light emitted by fluorescence, for example, cannot be recorded. Instead, in this work, we offer a theoretical discussion on why entropy minimization works in detecting the focal distance, together with comparisons with other focus metrics to validate the efficacy of this approach. In the following sections, we illustrate how to estimate the best depth for each pixel in reconstruction with the help of entropy.

From the viewpoint of information theory, the phenomenon of defocus in imaging can be considered in terms of filtering out high spatial frequencies. This increases the statistical correlation among neighboring sampling points. As the local randomness decreases, the waveform describing the image intensities becomes more predictable. In other words, when the sharpness of an image decreases, its information content is reduced consequently. Therefore, it is possible to compare the information content to measure the extent of defocus [22].

Normally the information content can be measured by Shannon entropy. The larger the entropy a message has, the more the information, or the larger the unpredictability of its probability distribution, that it contains. As such, we can use entropy to measure the sharpness of an image, and then use this to detect the focal distance [23,24]. For an image of $M \times N$ pixels, this is computed as

$$\mathcal{E} = -\sum_{x=1}^{M}\sum_{y=1}^{N}\frac{|R(x,y)|^2}{P}\log_2\frac{|R(x,y)|^2}{P}, \tag{2}$$

where $R(x,y) = \mathrm{Re}\{r(x,y)\}$ is the real part of the complex reconstruction $r(x,y)$, $P = \sum_{x=1}^{M}\sum_{y=1}^{N}|R(x,y)|^2$ is the total power of an image, and $\mathcal{E}$ is the entropy of this image.

To show that the entropy of reconstruction is minimal when the reconstruction distance is equal to the recording distance, we assume that the object has only one point at (x_0, y_0) on the z_0 plane, which can be represented as an impulse function $\delta(x_0, y_0; z_0)$. Theoretically, the reconstruction should also be a point if the reconstruction distance $z_r = z_0$ (neglecting aberration and finite aperture), because $h(x,y;z_0) * h^*(x,y;z_r)|_{z_r=z_0} = h(x,y;z_0) * h(x,y;-z_0) = \delta(x,y)$ according to Eq. (1) [4]. The probability distribution of the image is thus a Dirac delta function at x_0, which is deterministic. Consequently, the Shannon entropy $\mathcal{E} = -\sum_{i=1}^{N} p_i \log_2 p_i = 0$, where $p_i = 1$ is the probability distribution function.

When $z_r \neq z_0$, the reconstruction is blurred due to defocus, and its energy is spread over the space according to the radially symmetric PSF [22]. The probability density function of the energy is not a delta function, and, therefore, the entropy of the reconstruction is always larger than 0.

C. Example

According to this guideline, we give an example of detecting the focus location for the two-sectional object in Fig. 1(b). The autofocusing result is shown in Fig. 2.

As stated above, focus detection aims to determine the exact distance of each section, i.e., the circle and the rectangle. The computational process using entropy minimization is described below. First, the hologram is deconvolved using the conventional reconstruction method with multiple conjugate PSFs along z axis in a range of 1–25 mm. This range is determined from *a priori* knowledge about the location of the object. For each complex reconstruction, we compute the entropy of the real part, obtaining an entropy curve as shown in Fig. 2. The horizontal axis is the reconstruction distance in unit of millimeters, and the vertical axis is the normalized entropy in unit of bit. Then for this case, two local minimum points arrive at $z_1 = 10$ mm and $z_2 = 20$ mm. Therefore, we can assert that two separate sections are located at different depths in the 3D space. Based on this principle, we extend the concept of focus detection from an image to every pixel. In other words, we use entropy minimization to determine the best in-focus position for every pixel in the reconstructions.

3. EFI AND DM RECONSTRUCTIONS

To reconstruct an EFI image where each section is in focus, we first create a DM per pixel [25]. First, the complex hologram $g(x,y)$ is deconvolved with multiple PSFs along z axis, from $z_1, z_2, \ldots, z_k$, to obtain a stack of k reconstructions. Consequently, we have a volume of reconstructions $r(x,y,z)$, which is a 3D matrix with a size of $M \times N \times k$, and its real part is denoted as $R(x,y,z)$.

Then we search the in-focus position for each pixel based on entropy minimization. Since normally the entropy of an image is computed within a 2D area, for an individual pixel, we need to include its neighbors as a block with a specified size. This block size is assumed to be $L \times L$, where L is odd to ensure that the target pixel is located at the center, and for convenience, we define $\hat{L} = (L-1)/2$.

For any pixel (u,v), the entropy in each overlapping block corresponding to the axial distance z_i is computed as

$$\mathcal{E}(u,v,z_i) = -\sum_{x=u-\hat{L}}^{u+\hat{L}}\sum_{y=v-\hat{L}}^{v+\hat{L}}\frac{|R(x,y,z_i)|^2}{P}\log_2\frac{|R(x,y,z_i)|^2}{P}, \tag{3}$$

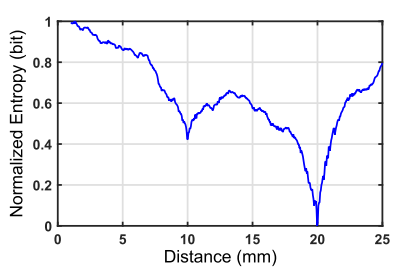

Fig. 2. Focus detection based on entropy minimization for the two-sectional object.

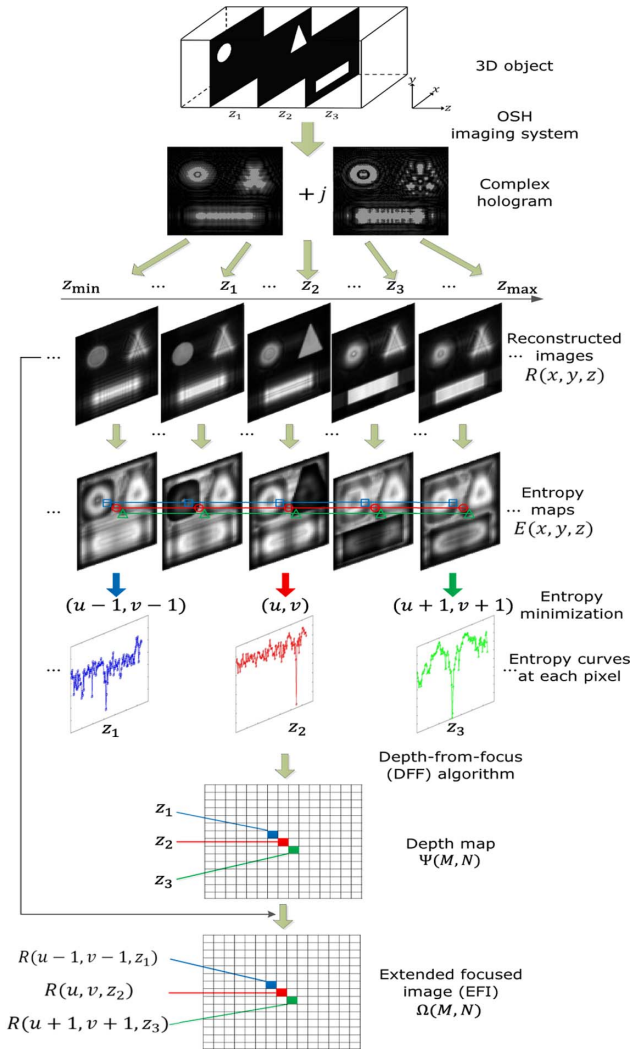

Fig. 3. Computational procedure of our proposed EFI approach.

where P is the power of $R(x, y, z_i)$ within the $L \times L$ block. This is computed for every pixel for each axial distance to obtain a full 3D matrix $\mathcal{E}(x, y, z)$.

Next we compute the DM $\Psi(x, y)$, which is a 2D image with pixel values representing the depth of the object. This is obtained by finding the minimum entropy along z-direction, i.e.,

$$\Psi(x, y) = z_i = \arg\min_z \mathcal{E}(x, y, z). \tag{4}$$

Accordingly, the EFI image, denoted as $\Omega(x, y)$, is obtained as

$$\Omega(x, y) = R(x, y, \Psi(x, y)). \tag{5}$$

The overall procedure of our proposed technique is illustrated in Fig. 3.

4. RESULTS AND ANALYSIS

A. Simulation

In the simulation, the two test objects consist of two and three dominant sections, as shown respectively in Figs. 1(b) and 1(c). The holograms are 256×256, with a block size of $L = 33$. In the first case, two transparent geometrical structures, a "circle" and a "rectangle," are located at 10 and 20 mm, respectively. In the second case, the same two patterns and a "triangle" are located at 10, 15, and 20 mm, respectively. The depth range in the two reconstructions is 8–22 mm, with 128 steps; thus, the interval between two scanning steps is about 0.11 mm.

Figure 4 shows the simulation results of the EFI images with two-sectional and three-sectional objects. From the comparison of the projection and EFI images in Figs. 4(a) and 4(b), we can see that all sections of the 3D object are reconstructed clearly and sharply. All sectional information appears in one single image without distortion of defocus noise, although some errors, which mainly come from the distortion between sections and around edges, partially contaminate the EFI image, as shown in the figures in the local magnification in Fig. 4. However, the artifacts do not influence the extension of the DOF and the reconstruction of the EFI image. The final all-in-focus EFI image enables more flexibility to analyze and visualize the recorded 3D object.

In simulation, it is easy to obtain a projection image containing all the sections, as shown in Fig. 4, and the ground-truth image that presents the exact depths of each section, as shown in Figs. 5(a) and 5(b). Figures 5(c) and 5(d) give the reconstructed 2D DM images. The colors in the 2D DM images represent the depth information of that pixel, and the color bar shows the accurate depth value. The two reconstructed 3D scenes shown in Figs. 5(e) and 5(f) illustrate the relative positions of the two recorded objects in 3D space. From the results, we see that the depths of most points are estimated correctly. However, the estimated depths of those pixels at the edges of each transparent region are not as accurate as that of the pixels inside. This is due to the focus detection procedure for every pixel. Since the entropy is computed in a block, for pixels in the peripheral area, the block has to incorporate the background pixels of the opaque region. The distortion introduced by a background pixel will lead to an error in the depth estimation of the center pixel.

B. Experimental Results

To validate the proposed approach, we also reconstruct the EFI and DM images using two experimental data sets used in some earlier publications [4,14].

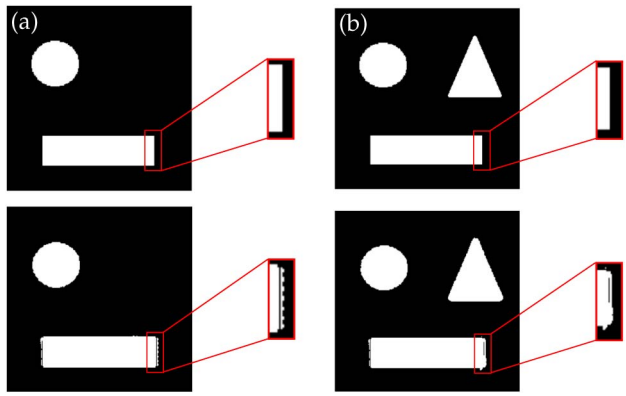

Fig. 4. (a) Top: the projection of the two-sectional object and local magnification; bottom: the EFI image and local magnification. (b) Top: the projection of the three-sectional object and local magnification; bottom: the EFI image and local magnification.

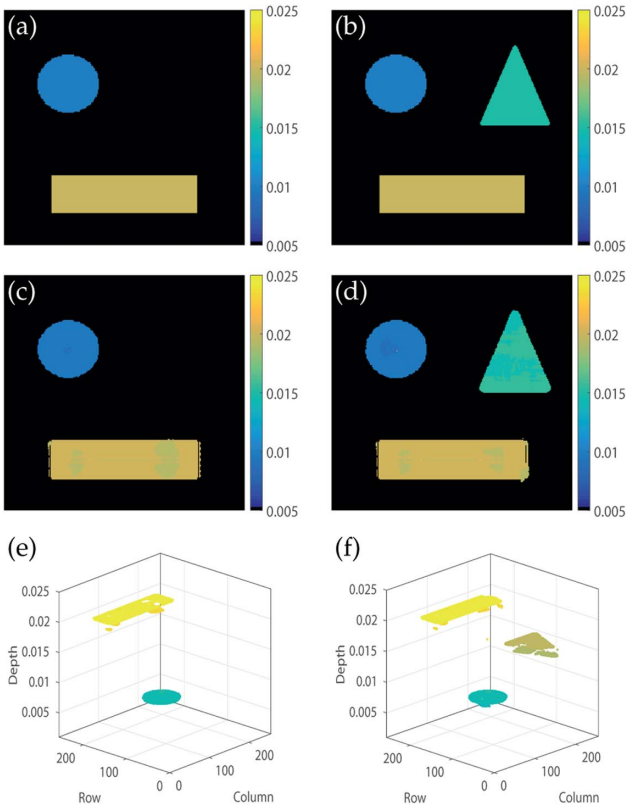

Fig. 5. (a, b) Ground-truth images of the two-sectional and three-sectional objects. (c, d) Reconstructed 2D DMs. (e, f) Reconstructed 3D scenes.

1. Two Transparencies

The first recorded 3D object consists of two transparencies containing the letters "S" and "H" [14]. Figure 6 shows the real and imaginary parts of the complex hologram.

We implement the proposed approach to reconstruct the EFI and DM images. The parameters are adjusted according to the analysis above. Reconstructed results are presented in Fig. 7. In conventional reconstruction shown in Fig. 7(a), the two letters are both blurred. In Fig. 7(b), the two dominant sections are reconstructed simultaneously in one single image. Defocus noise does not severely distort the reconstructions. As shown by the color bar in Fig. 7(c), the section with the letter "H" is located closer to the scanner than the other section with the letter "S." Figure 7(d) gives the reconstructed 3D scene of the original recorded object.

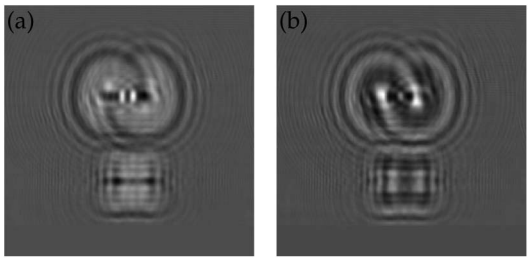

Fig. 6. (a) Real and (b) imaginary parts of the complex holograms of two transparent letters. They are the same as in Fig. 2 from [14], but are shown here also for ease of subsequent discussions.

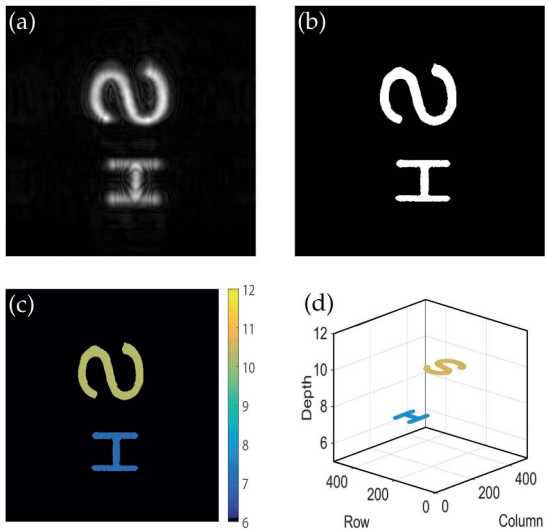

Fig. 7. (a) Conventional reconstruction at a middle section, and (b) an EFI image. (c) Reconstructed 2D DM images and (d) a 3D scene of "S" and "H."

2. Fluorescent Beads

The second test 3D specimen is a slice of fluorescent beads. The beads are located at distances from 70 to 125 μm. Detailed descriptions about the property of fluorescence and recording devices can be found in [4]. Figure 8 shows the real and imaginary parts of the complex hologram.

In Fig. 9, we show the reconstruction results acquired by the conventional approach at a middle section of 100 μm and by the proposed method. Figure 9(c) shows the two intensity distributions along the red lines in Figs. 9(a) and 9(b). Due to the defocus noise, background regions with no bead also have intensities acting as noise in the conventional reconstruction, as the blue curve depicts. On the other hand, in the EFI image, the defocus noise is extremely suppressed, and we can observe one specific bead with better resolution. This can also validate the suppression of defocus noise and enhancement of lateral resolution in the EFI image.

In Fig. 10, we present the reconstructed 2D DM image and 3D scene of the beads. The unit of the color bar is micrometers. From the DM image, we can see that the fluorescent beads are randomly distributed. There are more beads located at around 85 and 120 μm since points with these two colors are more than others in Fig. 10(b). This illustrates the description of two dominant sections given in [4]. However, it is worth noting

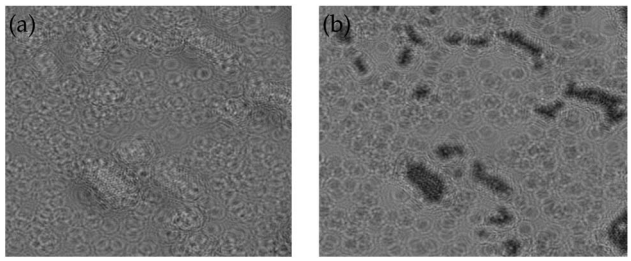

Fig. 8. (a) Real and (b) imaginary parts of the complex holograms of fluorescent beads.

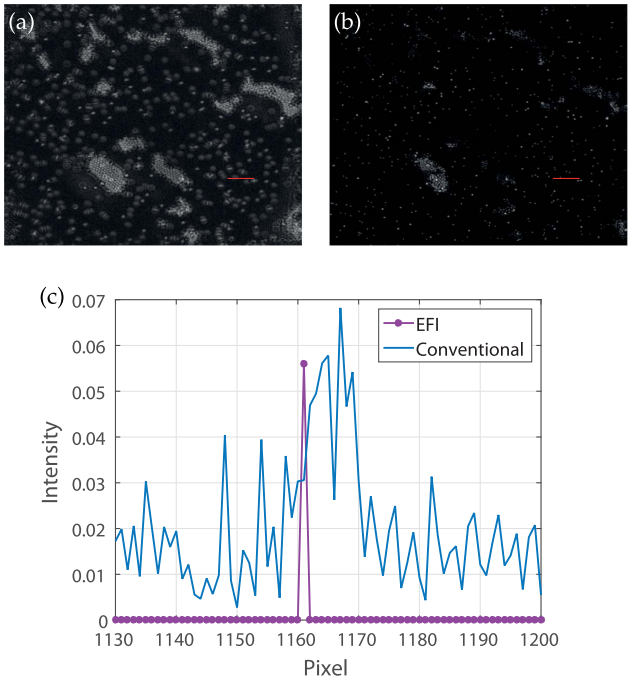

Fig. 9. (a) Conventional reconstruction at 100 μm. (b) Reconstructed EFI image. (c) Intensity profiles along the red lines in (a) and (b).

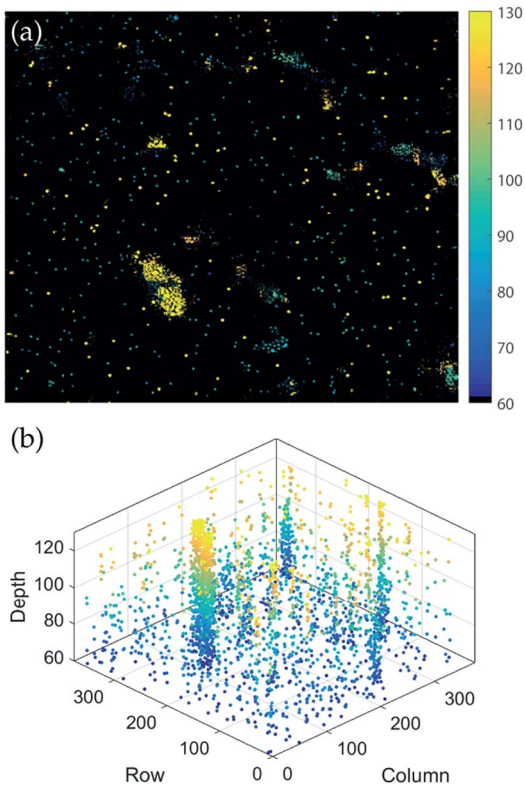

Fig. 10. (a) DM image of fluorescent beads. (b) Reconstructed 3D scene in space.

that artifacts may arise due to the pixel-by-pixel calculation for particle analysis. In this approach, we regard every pixel as one particle. This assumption is fine when the particles are small. For large particles that occupy several pixels, particles that actually do not exist will be incorrectly generated, and, therefore, artifacts become non-negligible in this case. This problem can possibly be solved if the single-molecule localization algorithm is used, or the calculation of the entropy is based on a region rather than a pixel.

C. Sectional Image Reconstruction

As achieved in confocal microscopy, optical sectioning refers to acquiring an image of a thick specimen by removing out-of-focus light from other image planes [14]. Instead of obtaining one single image in which every section is in focus, a sectional image only presents one specific section of the specimen, whereas other sections have no contribution. In the proposed method, we can also obtain sectional images easily from the DM of the recorded object. For each sectional image, a depth threshold is selected to partition the DM image into separate subimages, which only contain one specific section. Figure 11 presents some results obtained from simulation and experimental data.

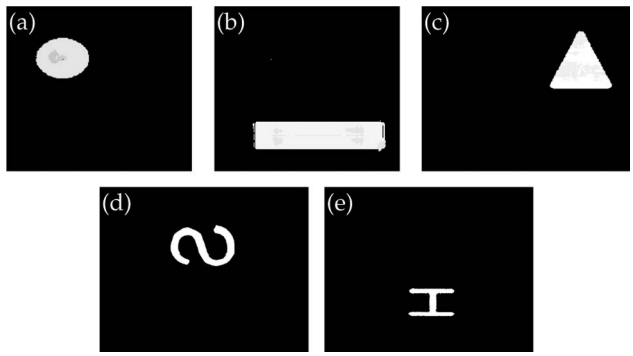

Fig. 11. Reconstructed sectional images of (a) a "circle," (b) a "rectangle," and (c) a "triangle" from simulation data, and (d) "S" and (e) "H" from experimental data.

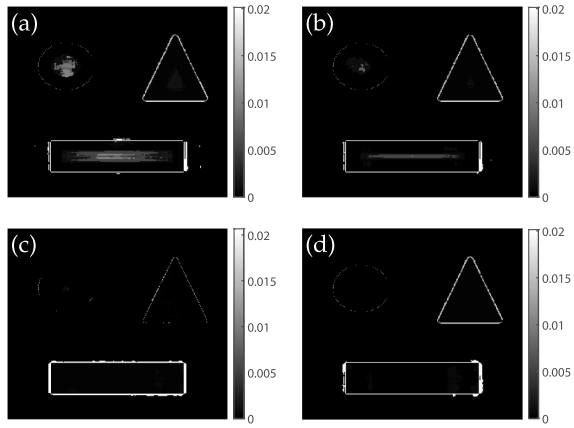

Fig. 12. Depth estimation error when the block sizes are (a) $L = 25$, (b) $L = 33$, (c) $L = 41$, and (d) $L = 49$, for the three-sectional object.

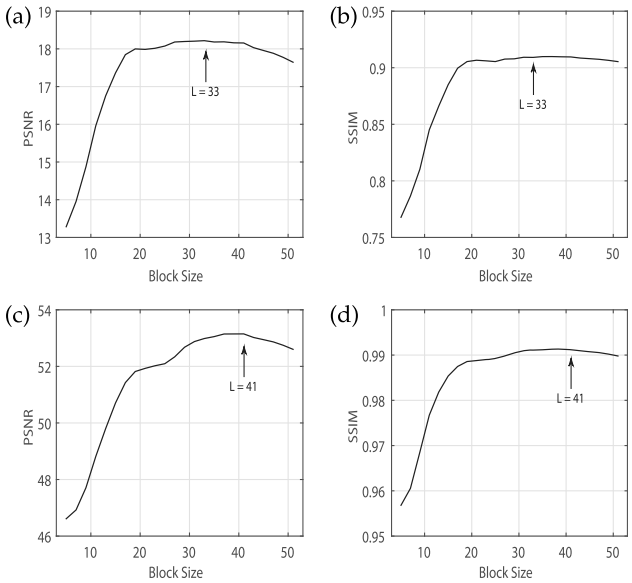

Fig. 13. (a, b) PSNR and SSIM curves of the EFI images versus block size. (c, d) PSNR and SSIM curves of the DM images versus block size.

With the estimated depth of each section, a sectional image can be reconstructed accordingly. Compared with conventional reconstructions, sectional reconstructions suffer little defocus noise originating from other sections. The focused sections are recovered in the respective sectional images.

D. Discussion on Block Size

The block size can affect the reconstructions of both EFI and DM images. For the object with three sections, we test the reconstructed image quality against different block sizes. Figure 12 gives the error of the reconstructed DM image and ground-truth image when the block sizes are 25, 33, 41, and 49.

Figure 13 shows the peak signal-to-noise ratio (PSNR; unit, decibel) and structural similarity (SSIM) [26] curves of the reconstructed EFI against the projection image, and the DM against the ground-truth image, as the block size ranges from 5 to 51. Since the PSNR has been proven to be inconsistent with human visual perception, we also employ SSIM, which is a perception-based model, to help justify the reconstructed image quality. For the EFI images, the PSNR and SSIM reach the peak when $L = 33$, and for the DM images, they are the largest when $L = 41$. If the block size continues to increase, the quality of both reconstructed images will decrease a bit. Therefore, we need to carefully select the size of the block in order to find a proper balance between the reconstructed EFI and DM image quality.

E. Comparison with Other Focus Metrics

As mentioned above, many focus metrics have been proposed to evaluate the focus status of an image. In essence, they can be categorized into four groups: derivative-based, histogram-based, power-based, and statistics-based [27]. Entropy belongs to the second family. In this section, we select Tenenbaum gradient, image power, variance, as well as wavelet to compare the

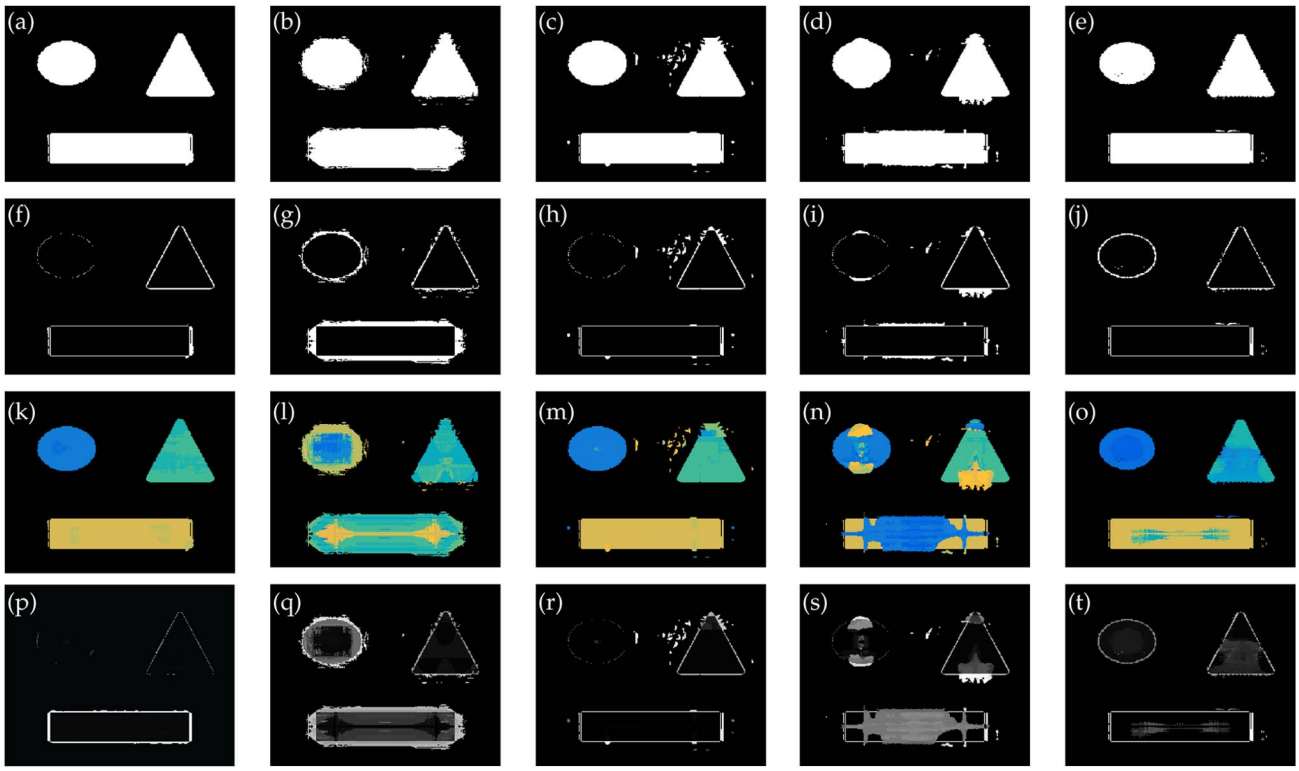

Fig. 14. Comparison of the reconstructed EFI and DM images, as well as the EFI and DM error images, produced by each metric. From left to right, the metrics are entropy, Tenenbaum gradient, image power, variance, and wavelet. (a)–(e) EFI images. (f)–(j) EFI error images. (k)–(o) DM images. (p)–(t) DM error images.

Table 1. PSNR and SSIM Values of the EFI against the Projection Image, and the DM against the Ground-Truth Image Produced by different Focus Metrics

	EFI		DM	
Metric	PSNR	SSIM	PSNR	SSIM
Entropy	18.2	0.9095	53.1	0.9912
Tenenbaum gradient	12.1	0.8083	47.2	0.9548
Image power	16.7	0.8695	51.4	0.9857
Variance	15.0	0.8621	47.5	0.9675
Wavelet	16.9	0.8800	52.4	0.9889

efficacy of detecting the focal distance in this application. In Fig. 14, we show the EFI and 2D DM images, along with the error images produced by each metric with the same parameters.

As we can see in Fig. 14, all the focus metrics can construct the EFI and DM. However, entropy produces the best image quality and the least error compared with the others. To quantitatively measure how much error the EFI and DM contain compared with the projection image and the ground-truth image, which are shown in Figs. 4(b) and 5(b), respectively, we calculate the PSNR and SSIM values. The results are shown in Table 1.

5. CONCLUSIONS

In DHM, one single image in which each section is in focus, and one DM that shows the depth information of the specimen, is highly desirable. In this paper, we propose an approach that can reconstruct the extended focused image and DM in an OSH imaging system. This method avoids extra optical components in the imaging system, as well as the time-consuming mechanical scanning procedure during recording. The reconstructed EFI shows the numerical extension of the DOF and presents each section clearly and sharply in one single image. In addition, the DM gives the locations of individual sections in 3D space. Simulation and experimental results verify the proposed approach. We also compare our method, entropy minimization, with other focus metrics and the results also show the efficacy against others. This approach can facilitate the visualization and measurement of microscopic objects in a holographic microscopy imaging system.

Funding. National Natural Science Foundation of China (NSFC) (N_HKU714/13); Research Grants Council (RGC); Research Grants Council of the Hong Kong Special Administrative Region, China (7131/12E).

REFERENCES

1. B. W. Schilling, T.-C. Poon, G. Indebetouw, B. Storrie, K. Shinoda, Y. Suzuki, and M. H. Wu, "Three-dimensional holographic fluorescence microscopy," Opt. Lett. **22**, 1506–1508 (1997).
2. T. Kim, "Optical sectioning by optical scanning holography and a Wiener filter," Appl. Opt. **45**, 872–879 (2006).
3. H. Kim, S.-W. Min, B. Lee, and T.-C. Poon, "Optical sectioning for optical scanning holography using phase-space filtering with Wigner distribution functions," Appl. Opt. **47**, D164–D175 (2008).
4. E. Y. Lam, X. Zhang, H. Vo, T.-C. Poon, and G. Indebetouw, "Three-dimensional microscopy and sectional image reconstruction using optical scanning holography," Appl. Opt. **48**, H113–H119 (2009).
5. X. Zhang, E. Y. Lam, and T.-C. Poon, "Reconstruction of sectional images in holography using inverse imaging," Opt. Express **16**, 17215–17226 (2008).
6. E. R. Dowski and W. T. Cathey, "Extended depth of field through wave-front coding," Appl. Opt. **34**, 1859–1866 (1995).
7. G. Indebetouw, W. W. Zhong, and D. Chamberlin-Long, "Point-spread function synthesis in scanning holographic microscopy," J. Opt. Soc. Am. A **23**, 1708–1717 (2006).
8. M. Matrecano, M. Paturzo, and P. Ferraro, "Extended focus imaging in digital holographic microscopy: a review," Opt. Eng. **53**, 112317 (2014).
9. T. Pitkäaho and T. J. Naughton, "Calculating depth maps from digital holograms using stereo disparity," Opt. Lett. **36**, 2035–2037 (2011).
10. J. J. Zhu, L. Wang, R. G. Yang, J. Davis, and Z. G. Pan, "Reliability fusion of time-of-flight depth and stereo geometry for high quality depth maps," IEEE Trans. Pattern Anal. Mach. Intell. **33**, 1400–1414 (2011).
11. M. Antkowiak, N. Callens, C. Yourassowsky, and F. Dubois, "Extended focused imaging of a microparticle field with digital holographic microscopy," Opt. Lett. **33**, 1626–1628 (2008).
12. C. P. McElhinney, B. M. Hennelly, and T. J. Naughton, "Extended focused imaging for digital holograms of macroscopic three-dimensional objects," Appl. Opt. **47**, D71–D79 (2008).
13. D. Vollath, "Automatic focusing by correlative methods," J. Microsc. **147**, 279–288 (1987).
14. X. Zhang, E. Y. Lam, T. Kim, Y. S. Kim, and T.-C. Poon, "Blind sectional image reconstruction for optical scanning holography," Opt. Lett. **34**, 3098–3100 (2009).
15. T. Pitkäaho, M. Niemelä, and V. Pitkäkangas, "Partially coherent digital in-line holographic microscopy in characterization of a microscopic target," Appl. Opt. **53**, 3233–3240 (2014).
16. M. Liebling and M. Unser, "Autofocus for digital Fresnel holograms by use of a Fresnelet-sparsity criterion," J. Opt. Soc. Am. A **21**, 2424–2430 (2004).
17. W. C. Li, N. C. Loomis, Q. Hu, and C. S. Davis, "Focus detection from digital in-line holograms based on spectral norms," J. Opt. Soc. Am. A **24**, 3054–3062 (2007).
18. T. Kim and T.-C. Poon, "Autofocusing in optical scanning holography," Appl. Opt. **48**, H153–H159 (2009).
19. C. Y. Zhou and S. K. Nayar, "Computational cameras: convergence of optics and processing," IEEE Trans. Image Proc. **20**, 3322–3340 (2011).
20. A. Torralba and A. Oliva, "Depth estimation from image structure," IEEE Trans. Pattern Anal. Mach. Intell. **24**, 1226–1238 (2002).
21. W. Chen, C. G. Quan, and C. J. Tay, "Extended depth of focus in a particle field measurement using a single-shot digital hologram," Appl. Phys. Lett. **95**, 201103 (2009).
22. V. M. Bove, "Entropy-based depth from focus," J. Opt. Soc. Am. A **10**, 561–566 (1993).
23. Z. B. Ren, N. Chen, A. Chan, and E. Y. Lam, "Autofocusing of optical scanning holography based on entropy minimization," in *Digital Holography and Three-Dimensional Imaging* (2015), paper DT4A.4.
24. L. Xi, L. Guosui, and J. Ni, "Autofocusing of ISAR images based on entropy minimization," IEEE Trans. Aerosp. Electron. Syst. **35**, 1240–1252 (1999).
25. Z. B. Ren, N. Chen, A. Chan, and E. Y. Lam, "Extended focused imaging in a holographic microscopy imaging system," in *IEEE International Conference on Imaging Systems and Techniques* (2015), pp. 1–6.
26. Z. Wang, A. C. Bovik, H. R. Sheikh, and E. P. Simoncelli, "Image quality assessment: from error visibility to structural similarity," IEEE Trans. Image Proc. **13**, 600–612 (2004).
27. H. A. Ilhan, M. Doğar, and M. Özcan, "Digital holographic microscopy and focusing methods based on image sharpness," J. Microsc. **255**, 138–149 (2014).